

Spherical-wave AVO-modelling in elastic VTI-media

Arnim B. Haase and Charles P. Ursenbach

ABSTRACT

The AVO response of two-layer VTI models for AVO Class I is investigated. Graebner/Rueger reflection coefficients and the “Weyl-integral for anisotropic media” are utilized for the computation. Spherical wave results are compared with the plane-wave reflectivity. Depth dependence of spherical wave AVO is found to be strongest near critical angles, as was observed in the isotropic situation. Both C-wave AVO and P-wave AVO are more sensitive to changes in anisotropy than to changes in depth.

INTRODUCTION

Previous spherical wave AVO investigations by the authors are restricted to isotropic media (Haase, 2004; Haase and Ursenbach, 2004). However it is well known that in many situations anisotropy is present either in the form of apparent anisotropy caused by layering or intrinsic anisotropy caused by, for example, shale layers. This type of anisotropy is usually called VTI (transversely isotropic with a vertical axis of symmetry). Rock fractures can cause HTI (horizontal symmetry axis TI) or also orthotropic anisotropy and these are not considered in this study.

Early work on spherical wave AVO by Hron et al. (1986) investigates anisotropy using asymptotic ray theory. They note that “anisotropic media produce noticeable differences in both amplitude- and time-distance curves as a function of the degree of anisotropy”; they also show amplitude-distance plots.

Previous work by the authors involved plane wave particle motion reflection coefficients given by Zoeppritz’s equations and the Weyl/Sommerfeld integral for computing isotropic spherical-wave potentials. Plane-wave particle motion reflection coefficients for VTI media have been presented by Graebner (1992) and in refined form by Rueger (1996). The Weyl-integral for anisotropic media is given by Tsvankin (2001). Their “exact” equations are utilized in this study. Approximations are introduced by performing numerical integrations.

THEORY

The displacement from a point force located at the origin is given by the following summation over plane waves (Tsvankin, 2001; equations 2.1-2)

$$\mathbf{u}(t, \mathbf{x}) = \frac{1}{2\pi} \int_{-\infty}^{\infty} \mathbf{S}(\omega, \mathbf{x}) \Phi(\omega) e^{i\omega t} d\omega, \quad (1)$$

$$\mathbf{S}(\omega, \mathbf{x}) = -\frac{i\omega}{4\pi^2} \sum_{\nu=1}^3 \int_0^{\infty} \int_0^{2\pi} \mathbf{U}^{(\nu)}(\mathbf{p}) \times e^{-i\omega [p_0 r \cos(\phi - \alpha) + p_3^{(\nu)} z]} p_0 dp_0 d\phi \quad (2)$$

where $z = x_3$ is the vertical receiver coordinate, r is the horizontal offset, α is the source-receiver azimuth with respect to the x_1 -axis, $\Phi(\omega)$ is the Fourier transform of the source pulse, \mathbf{p} is the slowness vector with components $\{p_1 = p_0 \cos\phi, p_2 = p_0 \sin\phi, p_3\}$, and $\mathbf{U}^{(\nu)}$ is

the displacement vector. For VTI media, there is no dependence on azimuth and the integration over $d\phi$ can be carried out analytically.

An explosive source (point source) can be modeled by three force pairs (Aki and Richards, 1980). Applying moment tensor methods leads, in cylindrical coordinates, to

$$S_r = \frac{iB\omega^2}{4\pi c_{33}c_{55}} \int_0^\infty R_{PP}(p_0) J_1(\omega p_0 r) e^{-i\omega\xi(z+h)} \times \frac{p_0^2 [c_{55}p_0^2 + (c_{33} - [c_{13} + c_{55}])\xi^2 - \rho]}{\xi(\xi^2 - \eta^2)} dp_0 \quad (3)$$

$$S_\phi = 0$$

$$S_z = -\frac{B\omega^2}{4\pi c_{33}c_{55}} \int_0^\infty R_{PP}(p_0) J_0(\omega p_0 r) e^{-i\omega\xi(z+h)} \times \frac{p_0 [(c_{11} - [c_{13} + c_{55}])p_0^2 + c_{55}\xi^2 - \rho]}{(\xi^2 - \eta^2)} dp_0 \quad (4)$$

where $R_{pp}(p_0)$ and the vertical slownesses ξ and η are given from plane-wave analysis (Graebner, 1992; Rueger, 1996). Similar equations have been developed for the converted wave case. The mathematical details can be found in Ursenbach and Haase (2005).

The integrations shown in equations (3) and (4) compute particle motion, one frequency point at a time. Then we proceed as in the isotropic situation: When all frequency points have been computed for the desired output bandwidth, the time domain response is found by inverse Fourier transform, and quadrature traces are determined by Hilbert transform; from these two trace types spherical-wave amplitudes are calculated.

MODELLING

The same two-layer model as was utilized in the isotropic situation (Haase, 2004) is also employed in this study. The layer parameters are $\alpha_1 = 2000$ m/s, $\beta_1 = 879.88$ m/s, $\rho_1 = 2400$ kg/m³, $\alpha_2 = 2933.33$ m/s, $\beta_2 = 1882.29$ m/s and $\rho_2 = 2000$ kg/m³. As before, a 5/15-80\100 Ormsby wavelet is chosen as the source signature; a P-wave point source is assumed. VTI-type anisotropy of the top layer is introduced in two steps: weak anisotropy ($\varepsilon = 0.15$, $\delta = 0.05$) and moderate anisotropy ($\varepsilon = 0.3$, $\delta = 0.1$); the bottom layer is always assumed to be isotropic. VTI radiation patterns and free surface effects are ignored in this study.

The appearance of the computed AVO results depends on scaling. Spherical spreading must be compensated for if results are to be compared to plane-wave responses. The P-wave examples shown in this report give magnitude displays normalized to the response magnitude obtained when reflection coefficients R_{PP} in equations (3) and (4) are set to unity. When R_{PS} is set to unity for C-wave examples, the scaled result oscillates relative to the plane-wave result at small incidence angles. In this region geometrical spreading factors are computed (Krebes and Slawinski, 1991) and calibrated to plane wave responses. These calibrated geometrical spreading factors depart from unity R_{PS} scaling at large incidence angles. For the converted wave case the Figures shown give magnitude displays scaled by a combination of unity R_{PS} and calibrated geometrical spreading factors with a transition region at the midrange of incidence angles. Figures 1 give an example for this mode of scaling.

Figure 2 compares AVO Class I spherical C-wave responses for weak and moderate VTI. Figure 3 shows anisotropic plane wave comparisons. Figures 4 and 5 display the equivalent P-wave responses. Figures 6 and 7 demonstrate depth dependence of weak and moderate VTI spherical wave AVO. In computing these figures, actual particle motion is projected onto the ray direction for P-waves and onto the perpendicular to the ray direction for C-waves.

DISCUSSION AND CONCLUSIONS

Inspection of layer velocities given in the previous section shows an increase across the interface. Because of this velocity increase critical angles exist and head waves are generated for Class I AVO models. Increasing top layer VTI-type anisotropy decreases this velocity contrast and a shift of the critical point towards larger angles is expected. Figures 2 and 4 prove this to be the case. A similar shift can be observed in Figures 3 and 5, giving anisotropic plane wave comparisons. Note the indicated zero crossing in these AVO-magnitude displays. Increasing VTI-type anisotropy pushes this crossover point to ever higher angles, meaning the AVO gradient is decreasing for lower angles. The spherical wave VTI AVO depth dependence is displayed in Figures 6 and 7. For both weak and moderate anisotropy, larger depths “tweak” the AVO response near the critical point to lower angles toward a plane wave comparison. Both C-wave AVO and P-wave AVO are more sensitive to changes in anisotropy than to changes in depth.

In anisotropic materials particle motion is not in the propagation direction for P-waves or perpendicular to the propagation direction for S-waves. The terms used in the literature are quasi-P-waves (qP) and quasi-S-waves (qS). For the above displays the actual particle motion is projected onto the propagation direction (at the ray angle) for P-waves and onto the ray angle perpendicular for C-waves.

REFERENCES

- Aki, K.T., and Richards, P.G., 1980, *Quantitative Seismology: Theory and Methods: Vol. 1*, W.H. Freeman and Co.
- Graebner, M., 1992, Plane-wave reflection and transmission coefficients for a transversely isotropic solid: *Geophysics*, **57**, 1512-1519.
- Haase, A.B., 2004, Spherical wave AVO modeling of converted waves in isotropic media: 74th Ann. Internat. Mtg. Soc. Expl. Geophys, 263-266.
- Haase, A.B., and Ursenbach, C.P., 2004, Spherical wave AVO-modelling in elastic isotropic media: CREWES Research Report, **16**.
- Hron, F., May, B.T., Covey, J.D., and Daley, P.F., 1986, Synthetic seismic sections for acoustic, elastic, anisotropic, and vertically inhomogeneous layered media: *Geophysics*, **51**, 710-735.
- Krebes, E.S., and Slawinski, M.A., 1991, On raytracing in an elastic-anelastic medium: *Bulletin of the Seismological Society of America*, **81**, 667-686.
- Rueger, A., 1996, Reflection coefficients and azimuthal AVO analysis in anisotropic media: Ph.D. Thesis, Colorado School of Mines.
- Tsvankin, I., 2001, *Seismic signatures and analysis of reflection data in anisotropic media*: Pergamon.
- Ursenbach, C.P., and Haase, A.B., 2005, Derivation of generalized reflections from point sources in a two-layer VTI medium: CREWES Research Report, **17**.

ACKNOWLEDGEMENTS

The authors wish to thank Professor E. Krebes for his help with the theory. Support by the CREWES team and its industrial sponsorship is gratefully acknowledged.

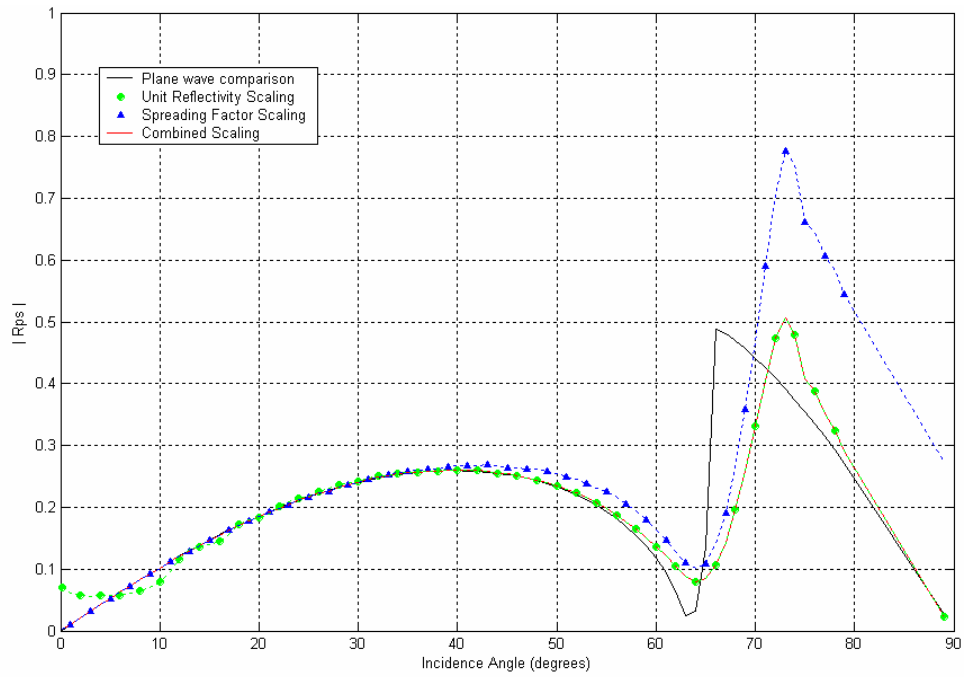


FIG. 1a. Spherical PS wave scaling example.

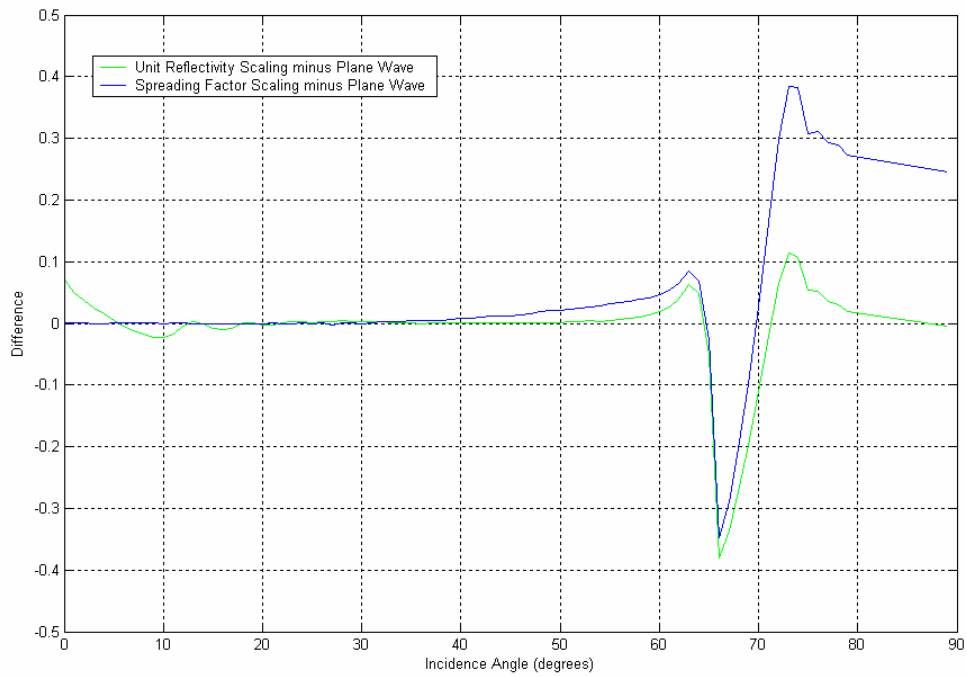


FIG. 1b. Difference plot for scaling example.

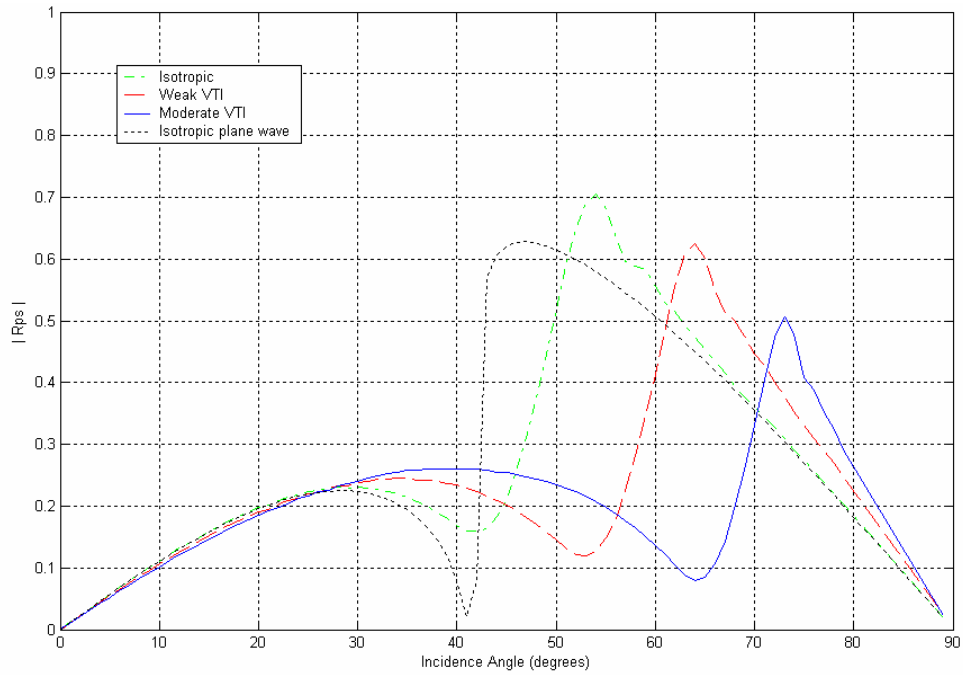


FIG. 2. VTI AVO-Class 1 spherical wave PS reflection coefficient (z=500m).

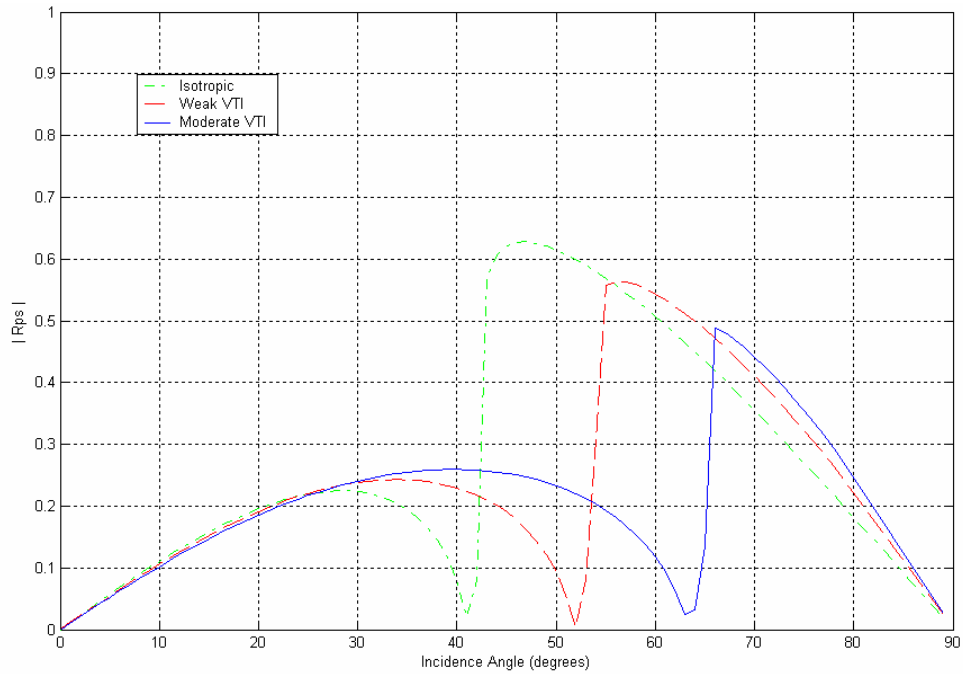


FIG. 3. VTI AVO-Class 1 plane wave PS reflection coefficient.

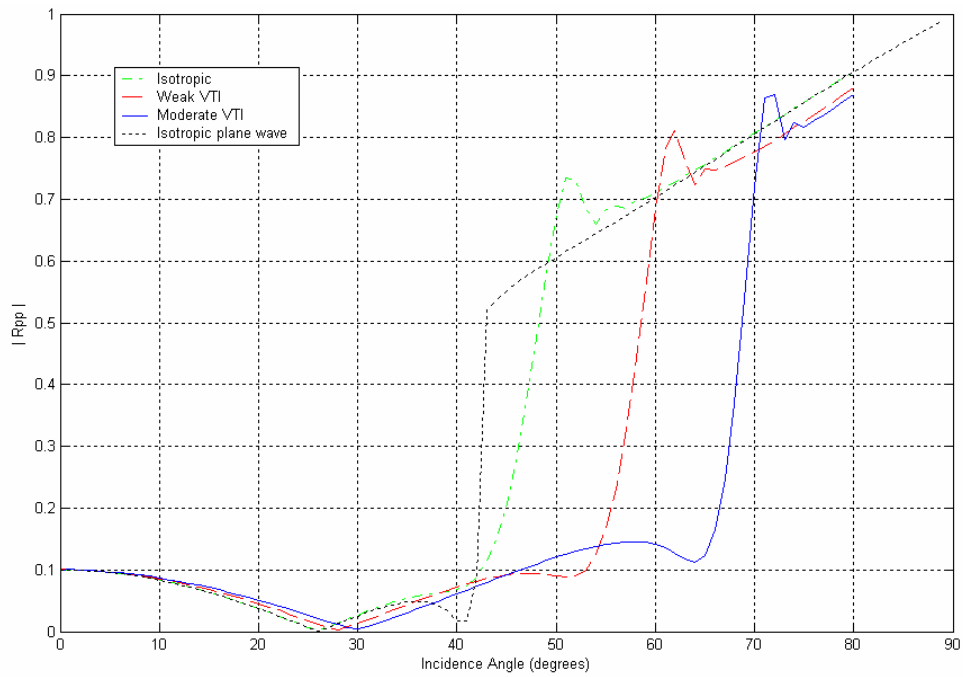


FIG. 4. VTI AVO-Class 1 spherical wave PP reflection coefficient ($z=500\text{m}$).

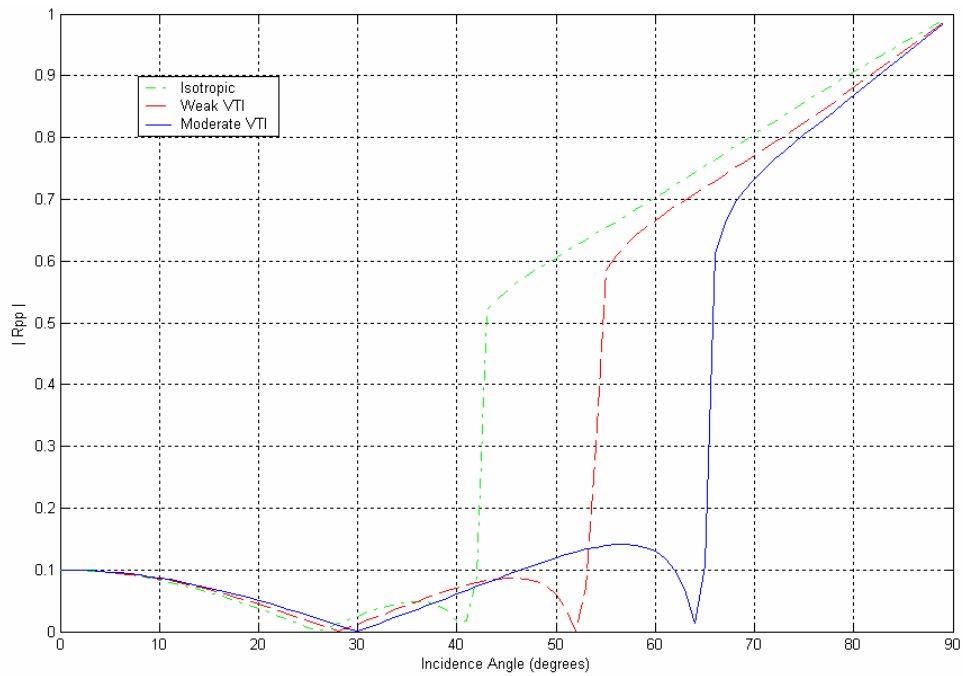


FIG. 5. VTI AVO-Class 1 plane wave PP reflection coefficient.

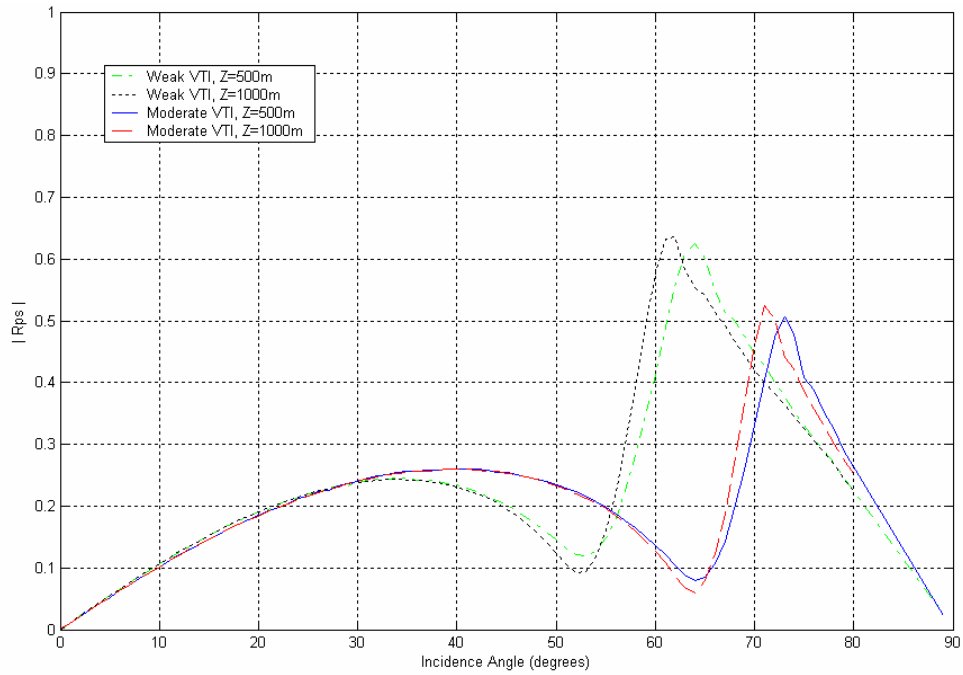


FIG. 6. VTI AVO-Class 1 spherical wave PS reflection coefficient.

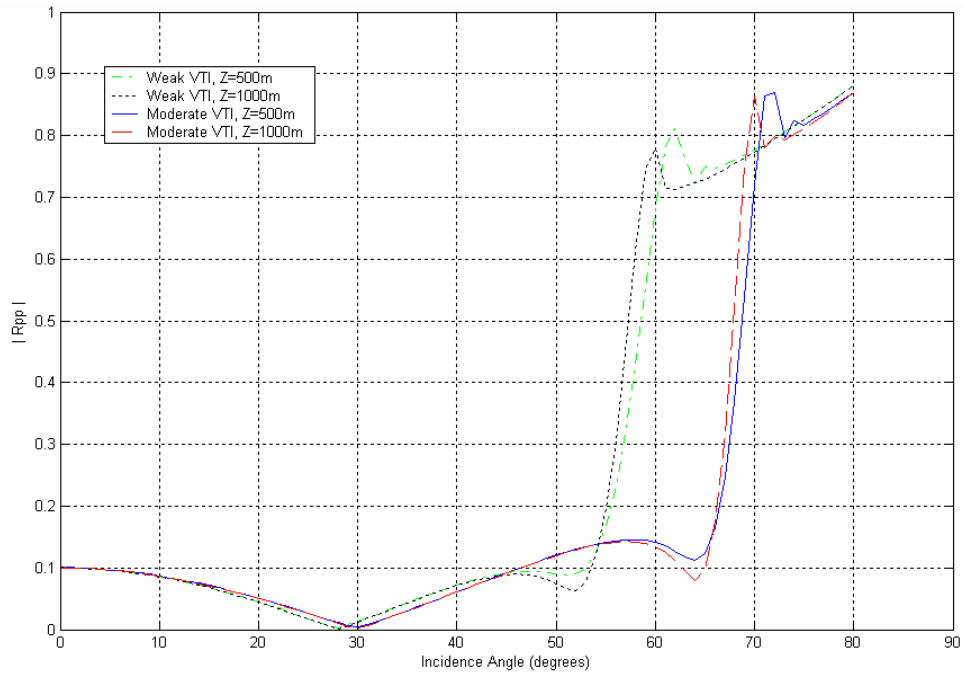


FIG. 7. VTI AVO-Class 1 spherical wave PP reflection coefficient.